metals

MDPI

Article

Achieving High Strength and Good Ductility in a Nb-Containing CoCrNi-Based High-Entropy Alloy by Grain Boundary and Precipitates Strengthening

Zewen Yu and Yaojun Lin *

School of Materials Science and Engineering, Wuhan University of Technology, Wuhan 430070, China; ze2073261@163.com

* Correspondence: yjlin@whut.edu.cn; Tel.: +86-139-7143-9387

Abstract: Face-centered cubic (FCC) high-entropy alloys (HEAs) have attracted considerable attention due to their excellent mechanical properties; however, an insufficient yield strength (YS) limits their widespread engineering applications. To improve the strength of FCC HEAs, the present work aims to develop fine-grained Nb-containing CoCrNi-based HEAs with precipitates. In the present work, a single-phase FCC $CoCrNi_{1.5}Nb_{0.2}$ HEA was processed by cold rolling followed by annealing at a higher temperature and aging at a lower temperature, yielding fine- and ultra-fine-grained FCC matrices and two types of precipitates: ultra-fine granular C15 Laves phase CoCrNb-based precipitates and ultra-fine lath-shaped $D0_{19}$-structured ε-Ni_3Nb-based precipitates. The resultant alloy exhibits a combination of high strength (approximately 1409 MPa of yield strength) and good ductility (10.1% of uniform elongation). The contributions of grain boundary and precipitation strengthening to YS were analyzed and calculated. The mechanisms underlying good ductility were discussed.

Keywords: high-entropy alloys; grain boundary strengthening; precipitation strengthening; strength; ductility

check for updates

Citation: Yu, Z.; Lin, Y. Achieving High Strength and Good Ductility in a Nb-Containing CoCrNi-Based High-Entropy Alloy by Grain Boundary and Precipitates Strengthening. *Metals* **2023**, *13*, 936. https://doi.org/10.3390/met13050936

Academic Editor: Andreas Chrysanthou

Received: 9 April 2023
Revised: 27 April 2023
Accepted: 8 May 2023
Published: 11 May 2023

Copyright: © 2023 by the authors. Licensee MDPI, Basel, Switzerland. This article is an open access article distributed under the terms and conditions of the Creative Commons Attribution (CC BY) license (https://creativecommons.org/licenses/by/4.0/).

1. Introduction

In recent years, a class of new alloys with complex, concentrated compositions, including high-entropy alloys (HEAs) and medium-entropy alloys (MEAs), have increasingly attracted attention due to their unique composition, microstructure and properties, such as high thermal and electrical conductivity, and excellent creep, corrosion, and wear resistance [1–6]. HEAs and MEAs comprise multiple principal elements with equiatomic or near-equiatomic fractions [5–8]. Usually, HEAs contain four or more principal elements, and MEAs include three elements [5–19]. Compared with conventional alloys that contain only a principal element, the unique compositional feature of HEAs and MEAs induces phenomena known as the "four core effects": high entropy, severe lattice distortion, sluggish diffusion and cocktail effects [20,21]. Interestingly, high entropy reduces Gibbs free energy (G = H-TS), which prevents the formation of intermetallics and retains and stabilizes a single-phase solid-solution structure [21–23]. To date, single-phase HEA solid solutions with three typical crystal structures have been reported, i.e., face-centered cubic (FCC), body-centered cubic and hexagonal close-packed structures [9,24–26].

Among a variety of HEAs/MEAs, FCC HEAs/MEAs exhibit significantly high ductility [27], damage tolerance [28] and superior irradiation and corrosion resistance [29,30]. Consequently, FCC HEAs/MEAs have received particular attention. However, their insufficient strength [31,32] confines their widespread engineering applications as structural materials. For example, the yield strength of single-phase CoCrNi [31] MEA and CoCrFeNiMn [32] HEA is below 400 MPa at room temperature. Therefore, it is important

to improve strength while retaining acceptable ductility. Various strengthening mechanisms, including solid-solution strengthening [33,34], dislocation and grain boundary (GB) strengthening [32,35–38] and precipitation strengthening [39–44], are employed to improve the strength of FCC HEAs/MEAs. For example, Yoshida et al. [37] prepared an ultra-fine-grained CoCrNi MEA single-phase solid solution with an average grain size of 199 nm via high-pressure torsion plus subsequent annealing, achieving a yield strength (YS) of 993 MPa but with a uniform elongation (UE) of 4.9%, compared to a YS of 270 MPa and UE of 54.2% in the coarse-grained counterpart (average grain size 111 μm). In another related study, Yang et al. [38] developed a three-level heterogeneous grain structure comprising nano-sized grains, ultra-fine grains and micrometric grains (with an average micrometric grain size of 2.3 μm) in CoCrNi MEA single-phase solid solution. As a result of GB strengthening, the YS reaches a value as high as 1150 MPa. Interestingly, the heterogeneous grain structure yields a UE as high as 22%. Hu et al. [45] introduced 3 at% Al and Mo into a CoCrNi MEA to form $(CoCrNi)_{97}Al_3$ and $(CoCrNi)_{97}Mo_3$ HEA single-phase solid solutions, respectively. The results show that, in $(CoCrNi)_{97}Al_3$ and $(CoCrNi)_{97}Mo_3$ HEAs with average grain sizes of 4.4–25.7 and 2.0–16.1 μm, Al and Mo solid-solution strengthening improves the YS by 43 and 79 MPa, whereas GB strengthening increases the YS by 119–316 and 176–474 MPa. By combining solid-solution and GB strengthening, the above two HEAs achieved 342–539 and 435–733 MPa YS with 62–79 and 49–74% elongation to failure. By adding Nb into the CoCrNi MEA, Zhou et al. [41] designed a HEA $CoCrNi_{1.5}Nb_{0.2}$ in order to increase the strength of CoCrNi MEA by precipitation strengthening. Depending on the aging temperature and time, precipitation strengthening of nanoscale γ'' coherent precipitates contribute to the YS by 835–953 MPa, whereas GB strengthening and solid-solution strengthening of Nb increases the YS by 119–125 MPa (with average grain sizes of 45.3–50.2 μm) and 23–37 MPa, respectively. The combination of precipitation, GB and solid-solution strengthening leads to YSs of 997–1182 MPa accompanied by a UE of 9.4–22%.

The above review on the effect of strengthening mechanisms on the YS of FCC HEAs/MEAs gives rise to two important observations: first, both grain boundary strengthening and precipitation strengthening can significantly improve the YS. In contrast, solid-solution strengthening provides only a modest contribution to the YS. This is probably because the elements that can generate effective solid-solution strengthening have limited solubility in HEA/MAE matrices [46]. Second, grain boundary strengthening can be significantly enhanced by decreasing the grain size, as described by the well-known Hall–Petch equation. Therefore, the combination of grain boundary strengthening of fine grains and even ultra-fine and nano-sized grains and precipitation strengthening should be able to significantly improve the YS of HEAs/MEAs. An inspection of the published studies shows that, to date, such a combined strengthening strategy has received limited attention [47–49]. In view of the above discussion, the objective of the present work is to improve the strength of the CoCrNi MEA through the combination of the grain boundary strengthening of fine or ultra-fine grains and precipitation strengthening. To do so, Nb is added into CoCrNi MEA to form CoCrNi-based $CoCrNi_{1.5}Nb_{0.2}$ HEA. The cast $CoCrNi_{1.5}Nb_{0.2}$ HEA is homogenized and solid-solution treated to obtain a single-phase FCC structure and then cold-rolled, followed by annealing and aging, forming Nb-rich precipitates dispersed in fine (defined as grain sizes of 1–10 μm) and ultra-fine (defined as grain sizes of 0.1–1 μm) grains. For the $CoCrNi_{1.5}Nb_{0.2}$ HEA produced, its microstructures are characterized, tensile properties are tested, and underlying mechanisms for strength and ductility are analyzed and discussed.

2. Materials and Methods

The elements Co, Cr, Ni and Nb, with a purity of >99.5 wt%, were used to prepare $CoCrNi_{1.5}Nb_{0.2}$ HEA ingots. In a water-cooled copper crucible under a high-purity argon atmosphere, the mixture of the elements Co, Cr, Ni and Nb was first arc melted to form a molten alloy, which was then solidified and cooled down to room temperature, producing the button-shaped ingots with a diameter of ~18 mm and thickness of ~6 mm. For the

purpose of compositional uniformity, each ingot was flipped and remelted at least four times. The button-shaped ingots were solid-solution treated and homogenized at 1200 °C for 20 h in an argon atmosphere to eliminate the micro-segregation of the composition and then water-quenched to form a single-phase solid solution. The homogenized (H) and solid-solution treated (SST) ingots were first cold-rolled (CR) from 6 mm to 0.9 mm in thickness, then annealed (AN) at 900 °C for 3 min, and finally aged (AG) at 660 °C for 18 h. The annealing condition of 900 °C for 3 min was selected in order to accomplish the goal of the present work to achieve high strength and ductility. When annealing at 800 °C for 1 h, a high strength (with a yield strength of 1401 MPa) was retained relative to that of the cold-rolled counterpart (with a yield strength of 1548 MPa) but with low ductility (uniform elongation 4.1%); when annealing at 1000 °C, a holding time of 3 min led to a significant decrease in the yield strength to 1100 MPa, albeit with a significant increase in ductility (uniform elongation of 20%), as shown in Figure S1. Thus, 900 °C for 3 min was chosen as the annealing condition, attempting to attain the combination of high strength and ductility.

X-ray diffraction (XRD) analysis was performed on the as-cast, H+SST, as-CR and CR+AN+AG $CoCrNi_{1.5}Nb_{0.2}$ HEAs in a Bruker D8 Advance diffractometer using Cu Kα radiation with the scanning rate of 4 /min and the scanning range of $2\theta = 20°–100°$. Microstructures in as-cast and H+SST $CoCrNi_{1.5}Nb_{0.2}$ HEAs were analyzed using a field emission gun (FEG) Gemini 300 scanning electron microscope (SEM) operated at 10 kV. The SEM samples were prepared by mechanical grinding from 400 to 2000 grit SiC sandpapers and then by electrolytic polishing in a solution of 10% $HClO_4$ and 90% C_2H_5OH under 30 V at room temperature. The microstructures in the as-CR and CR+AN+AG $CoCrNi_{1.5}Nb_{0.2}$ HEAs were analyzed using a transmission electron microscope (TEM) and scanning transmission electron microscope (STEM) FEI Talos F200X equipped with energy-dispersive X-ray spectroscopy (EDS) and operated at 200 kV. TEM/STEM analyses were performed on the longitudinal plane, determined by the rolling and normal directions. The TEM/STEM specimens were prepared by mechanical grinding to 30 μm, followed by twin-jet polishing to electron transparency in an electrolyte 90% C_2H_5OH and 10% $HClO_4$ under 30 V at −20 °C. The microstructures in the CR+AN+AG $CoCrNi_{1.5}Nb_{0.2}$ HEAs were also studied using electron backscatter diffraction (EBSD) in the FEI Quanta FEG 300 scanning electron microscope (SEM) equipped with an Oxford EBSD detector. The step size of the EBSD scans was 0.09 μm, and the acceleration voltage was 20 kV. The EBSD specimens were prepared by mechanical grinding first, then vibratory polishing, and finally electro-polishing in the same electrolyte as the aforementioned one for twin-jet polishing under 20 V for 30 s.

The tensile tests of the as-CR and CR+AN+AG $CoCrNi_{1.5}Nb_{0.2}$ HEAs were performed at room temperature with the initial strain rate of 5×10^{-4} s^{-1} using an Instron-5966 Tester equipped with a video extensometer, which was used to precisely measure the strains in the gauge section of a tensile specimen. Dog-bone-shaped specimens, with a normal length of 14 mm and a cross-section of 4 mm × 1 mm, were used. The loading direction was parallel to the rolling direction. The samples were cut by an electrical discharge machine and carefully mechanically polished. In order to ensure the reliability of the measured results, more than four specimens were tested for each type of the two alloys. The fractured surfaces of tensile specimens were observed using the above FEI Quanta FEG 300 SEM at 20 kV.

3. Results

3.1. Microstructural Characterization

Figure 1a is the XRD patterns of the as-cast, H+SST, as-CR and CR+AN+AG $CoCrNi_{1.5}Nb_{0.2}$ HEAs. All HEAs include an FCC phase. Based on the XRD pattern, the Nelson–Riley function [6,50] ($f(\theta) = (\cos 2\theta/\sin\theta + \cos 2\theta/\theta)/2$) extrapolation method was used to calculate the lattice constants of the FCC phase matrices of the four alloys. The lattice constants of the as-cast, H+SST, as-CR and CR+AN+AG $CoCrNi_{1.5}Nb_{0.2}$ HEAs were determined as 3.5842, 3.5864, 3.5862 and 3.5672 Å, respectively. Compared with the H+SST and as-CR HEAs (both

of them have almost the same lattice constants), a decrease in the lattice constants of the as-cast and CR+AN+AG HEAs suggests the presence of Nb-rich phases since the atomic radius of Nb (1.47 Å [42,51]) is larger than those of other elements (Co 1.25 Å, Cr 1.29 Å and Ni 1.25 Å [42,51]). Moreover, relative to the positions of the diffraction peaks in the as-CR and H+SST $CoCrNi_{1.5}Nb_{0.2}$ HEAs, the corresponding diffraction peaks in the as-cast and CR+AN+AG $CoCrNi_{1.5}Nb_{0.2}$ HEAs slightly shift to the right, i.e., to higher Bragg angles, suggesting reduced lattice constants and Nb-rich phase precipitation. Figure 1b shows an enlargement in the range of 2θ = 40–55°, more clearly illustrating peak shifting. In fact, in both the as-cast and CR+AN+AG HEAs, peaks other than those of the FCC phases can be seen, confirming the presence of the second phase. On the basis of the additional peaks in the XRD patterns in as-cast HEA, the second phase can be identified as δ-Ni_3Nb, with the tetragonal structure of lattice constants being a = 5.11 Å, b = 4.25 Å and c = 4.55 Å (JCPDF reference number 15-0101 [52]). Based on the additional peaks in the XRD patterns in CR+AN+AG HEA, two types of second phases can be detected. One type can be identified as ε-Ni_3Nb, with a hexagonal $D0_{19}$ structure of lattice constants of a = 5.190 Å and c = 8.384 Å (JCPDF reference number 15-0498 [53]), and another type is C15 Laves phase CoCrNb, with a hexagonal structure of lattice constants of a = 4.849 Å and c = 7.907 Å (JCPDF reference number 33-0391 [54,55]). In contrast, the H+SST and CR+AN+AG HEAs exhibit single-phase FCC structures. The δ-Ni_3Nb phase in the as-cast HEA was formed, probably during solidification and subsequent solid-state cooling. The ε-Ni_3Nb phase and CoCrNb Laves phase were obtained by precipitation during annealing and aging.

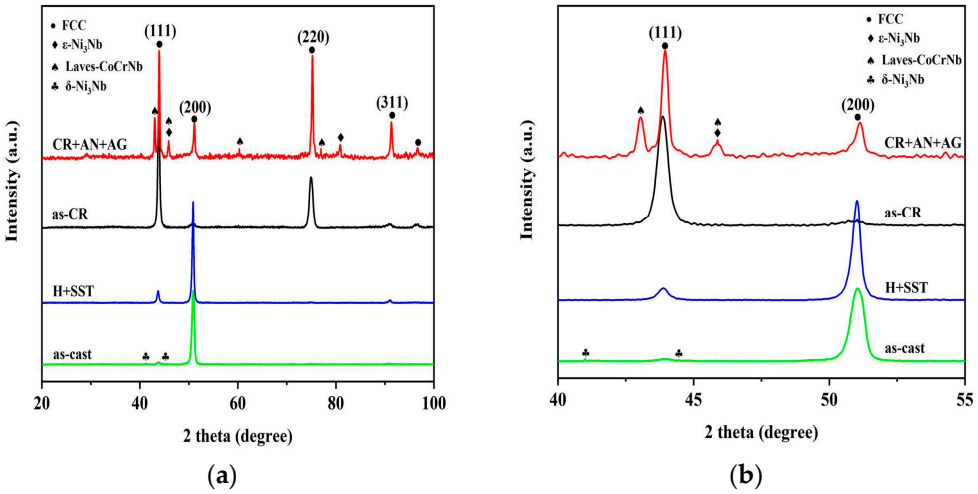
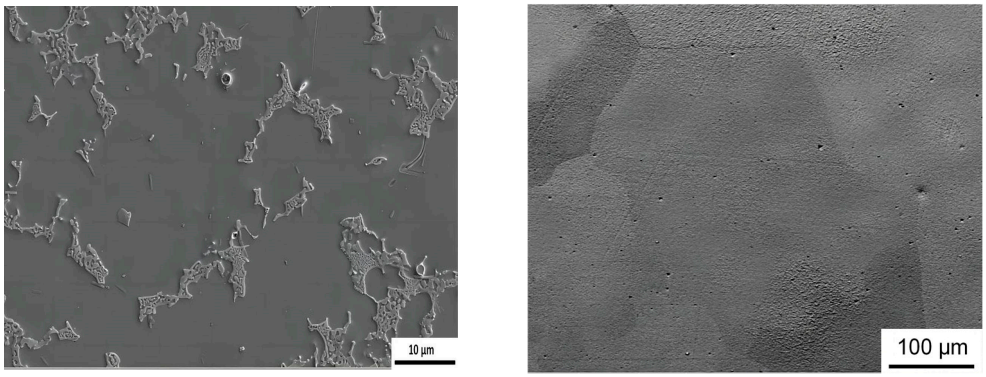


Figure 1. (**a**) The XRD patterns of as-cast, H+SST, as-CR and CR+AN+AG $CoCrNi_{1.5}Nb_{0.2}$ HEAs; (**b**) enlarged section in the range of 2θ = 40–55°.

The SEM micrograph in Figure 2a shows the microstructure of the as-cast $CoCrNi_{1.5}Nb_{0.2}$ HEA, comprising the matrix and eutectic microstructure distributed in the matrix. In terms of the above phase identification based on the XRD pattern, the matrix should be that of the FCC phase, and the eutectic microstructure should comprise the FCC phase and δ-Ni_3Nb phase. The SEM micrograph in Figure 2b shows a single-phase microstructure with grain sizes on the order of several hundred micrometers in H+SST $CoCrNi_{1.5}Nb_{0.2}$ HEA. By solid-solution treatment, the δ-Ni_3Nb phase was completely dissolved into the matrix, consistent with the above XRD result.

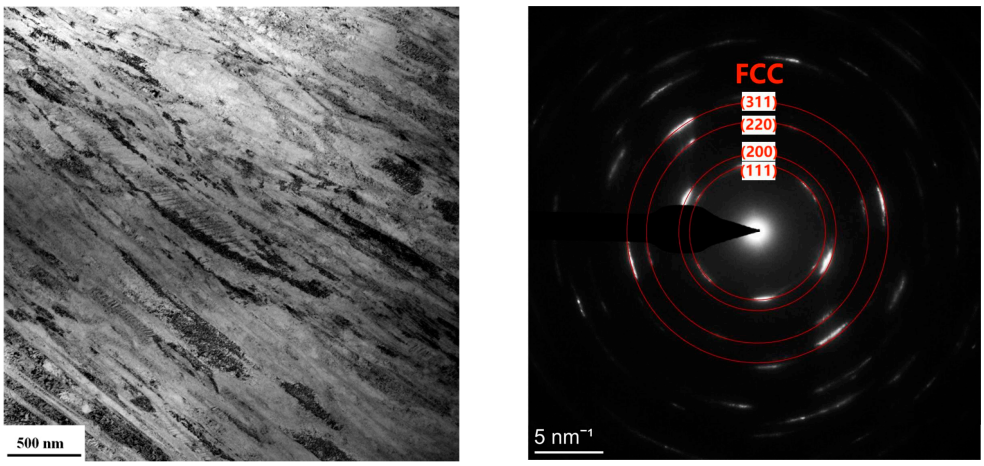
The TEM bright-field (BF) micrograph in Figure 3a shows the microstructure in the as-CR $CoCrNi_{1.5}Nb_{0.2}$ HEA, which is characterized by a nanoscale and ultra-fine lamellar structure. The ring-like selected area electron diffraction (SAED) pattern indicates the as-CR $CoCrNi_{1.5}Nb_{0.2}$ HEA to be an FCC single-phase solid solution, as shown in Figure 3b. The STEM angular bright-field (ABF) micrograph in Figure 4a demonstrates the microstructure in the CR+AN+AG $CoCrNi_{1.5}Nb_{0.2}$ HEA, and it comprises two types of precipitates: gran-

ular and lath-shaped precipitates distributed in the fine and ultra-fine grained matrices. These microstructural features are also displayed in the corresponding two different-angle angular dark-field micrographs in Figure S2a (DF2) and b (DF4) and the high-angle angular dark-field (HAADF) micrograph in Figure S2c. The sizes of the granular precipitates fall in the range of 90–420 nm. The widths and lengths of the lath-shaped precipitates range from 50–170 nm and 1.0–4.4 μm, respectively. The volume fractions of the granular and lath-shaped precipitates were measured to be 17.4% and 7.6%, respectively. The dimensions and volume fractions of the two types of precipitates are reported in Table 1. As shown in Figure 4b–e, the EDS mapping corresponding to Figure 4a shows the Nb- and Ni-rich features of the two types of precipitates. The compositions of the two types of precipitates and the matrix measured based on the EDS mapping are reported in Table 2. As shown in Figure 4f, the ring-like SAED pattern, taken from a randomly selected region of 4 μm in diameter (aperture diameter of 4 μm), supports the presence of fine or ultra-fine grains in the matrix. A careful inspection of Figure 4a shows a low density of dislocations in those fine and ultra-fine grains. Thus, the fine and ultra-fine grains were formed by recrystallization during annealing and aging, and simultaneously, the two types of precipitates were produced.



(**a**) (**b**)

Figure 2. The microstructure in $CoCrNi_{1.5}Nb_{0.2}$ HEA: (**a**) as-cast; (**b**) homogenized + solid-solution treated.



(**a**) (**b**)

Figure 3. The microstructure in as-CR $CoCrNi_{1.5}Nb_{0.2}$ HEA: (**a**) TEM BF micrograph showing nanoscale and ultra-fine lamellar microstructure; (**b**) SEAD pattern showing single-phase FCC solid solution.

Table 1. The dimensions and volume fraction of granular and lath-shaped precipitates in CR+AN+AG $CoCrNi_{1.5}Nb_{0.2}$ HEA.

Precipitates	Size (nm)	Width (nm)	Length (μm)	Volume Fraction (%)
Granular Precipitates	90–420	——	——	17.4
Lath-shaped Precipitates	——	50–170	1.0–4.4	7.6

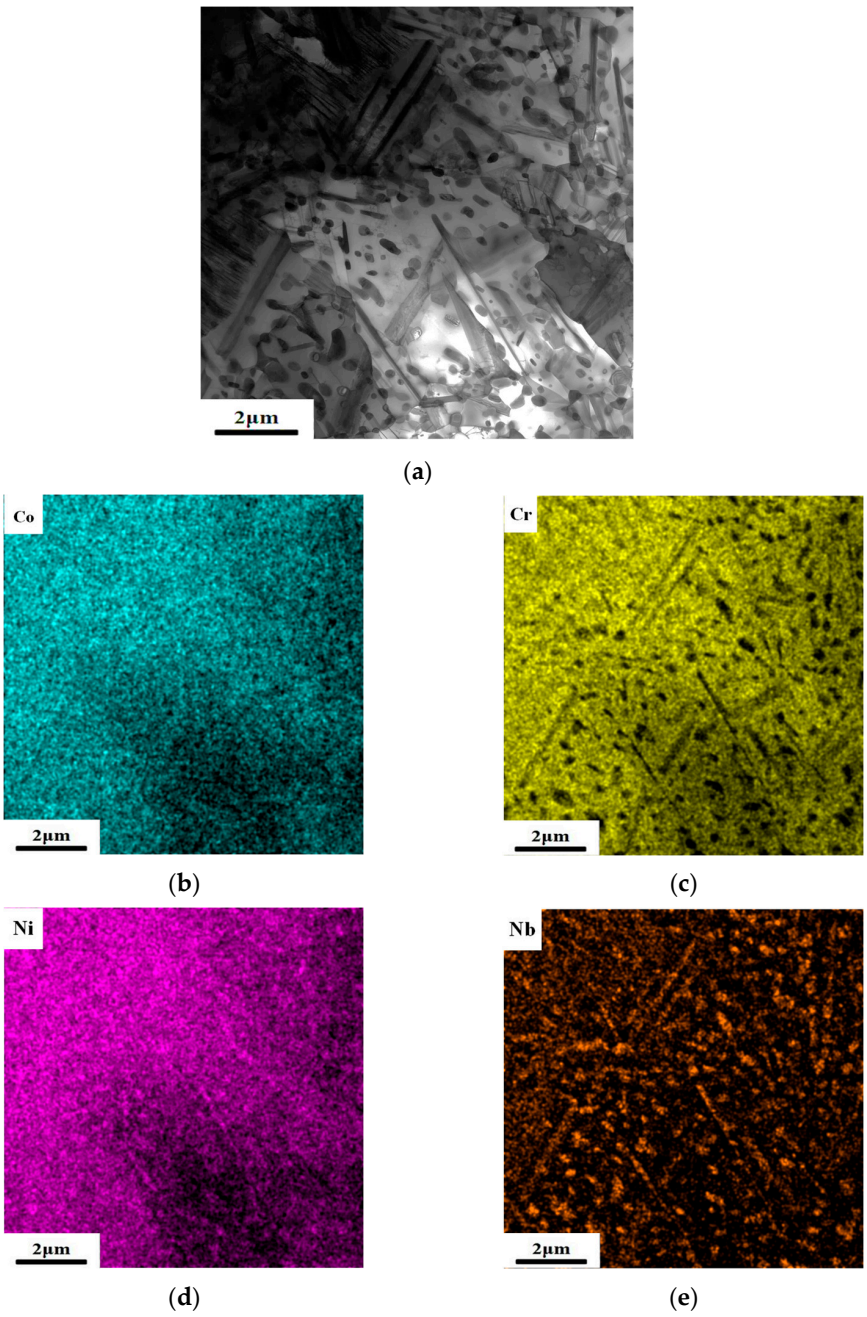


Figure 4. *Cont.*

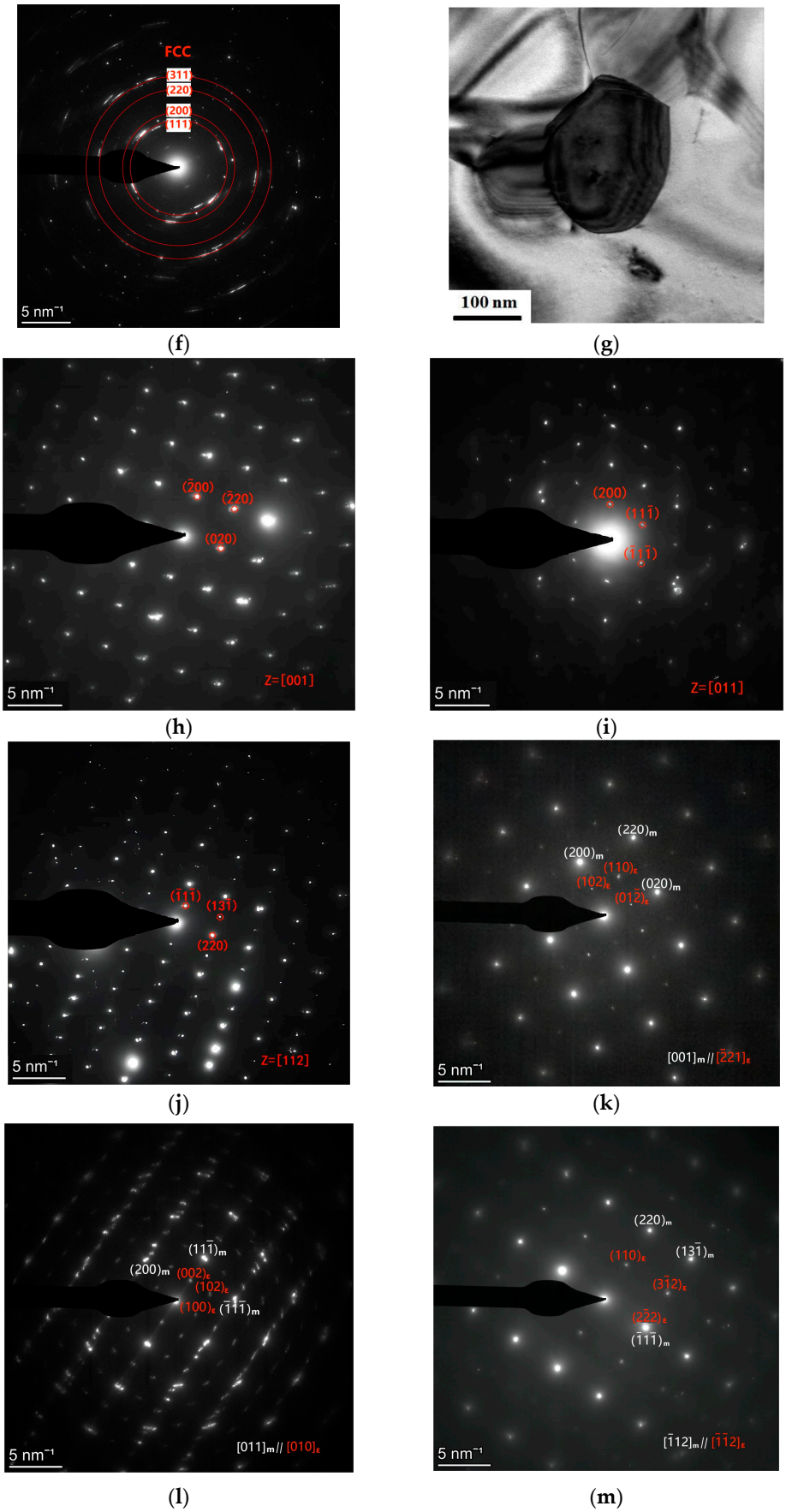
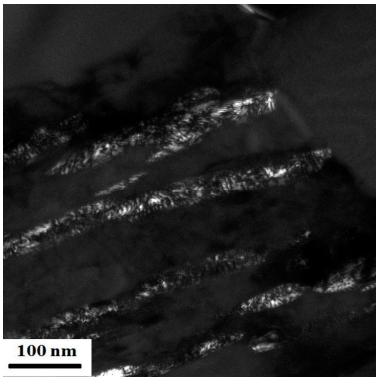


Figure 4. *Cont.*



(**n**)

Figure 4. Microstructures in the CR+AN+AG $CoCrNi_{1.5}Nb_{0.2}$ HEA: (**a**) STEM ABF; (**b**–**e**) STEM-EDS mapping corresponds to (**a**); (**f**) SAED pattern taken from a region of 4 μm in diameter; (**g**) TEM BF micrograph showing granular precipitates; (**h**–**j**) SAED patterns of a granular precipitate; (**k**–**m**) SAED patterns from the regions, including lath-shaped precipitates and the matrix; (**n**) TEM DF micrograph showing lath-shaped precipitates.

Table 2. The compositions of matrix and granular and lath-shaped precipitates in CR+AN+AG $CoCrNi_{1.5}Nb_{0.2}$ HEA measured by STEM-EDS (at%).

Phase	Co	Cr	Ni	Nb
Matrix	26.46 ± 0.31	31.02 ± 0.41	40.24 ± 0.44	2.28 ± 0.26
Granular precipitates	32.54 ± 0.41	6.68 ± 0.29	42.27 ± 0.61	18.51 ± 0.42
Lath-shaped precipitates	26.09 ± 0.29	7.23 ± 0.62	49.29 ± 0.32	17.39 ± 0.54

The higher magnification TEM BF micrograph in Figure 4g shows the microstructure of the granular precipitate in the CR+AN+AG $CoCrNi_{1.5}Nb_{0.2}$ HEA. Figure 4h–j shows the SAED patterns of the granular precipitate on the zone axes of [001], [011] and [112]. The indexing of these SEAD patterns indicates the nanoscale granular precipitates to be C15 Laves phases CoCrNb with a hexagonal structure of lattice constants of a = 4.849 Å and c = 7.907 Å, which is consistent with the result obtained from the X-ray diffraction [54,55]. Based on the composition in Table 2, Ni may replace a portion of Co, Cr and Nb, thus forming the CoCrNb-based (Co, Ni)(Cr, Ni)(Nb, Ni) phase. Figure 4k–m shows the SAED patterns taken from the regions, including the lath-shaped precipitates and the FCC matrix on the zone axes of [001] m, [011] m and [112] m of the matrix, with "m" denoting the matrix. In these SAED patterns, the larger and brighter spots and the smaller and weaker spots come from the FCC matrix and precipitates, respectively. The TEM dark-field (DF) micrograph in Figure 4n, which was acquired by imaging using the diffraction spots from the lath-shaped precipitates, shows the lath-shaped precipitates. By indexing those spots corresponding to the precipitates, the precipitates can be identified as a typical hexagonal ε-Ni_3Nb phase with a $D0_{19}$ structure (lattice constants of a = 5.190 Å and c = 8.384 Å) [53], which is consistent with the above XRD result. Based on the composition in Table 2, Co and Cr may replace Ni, and Cr may substitute Nb, forming ε-Ni_3Nb-based ε-$(Ni, Co, Cr)_3(Nb, Cr)$ phase [44,45]. Interestingly, the matrix and ε precipitates are coherent on the zone axes of [001] m and [112] m, whereas, in the zone axis of [011] m, the matrix and ε precipitates are incoherent, which is indicative of a semi-coherent relationship between the ε precipitates and the matrix.

In order to better highlight the grain morphology and size in the CR+AN+AG $CoCrNi_{1.5}Nb_{0.2}$ HEA, the EBSD inverse-pole figure map is demonstrated in Figure 5a, confirming the presence of fine and ultra-fine grains. By fitting the grain size distribution using a log-normal probability function, the average grain size is estimated as $d = 1.15^{+0.32}_{-0.19}$ μm, i.e., the average grain size of 1.15 μm with upper and lower standard deviations of +0.32 and −0.19 μm, as shown in Figure 5b.

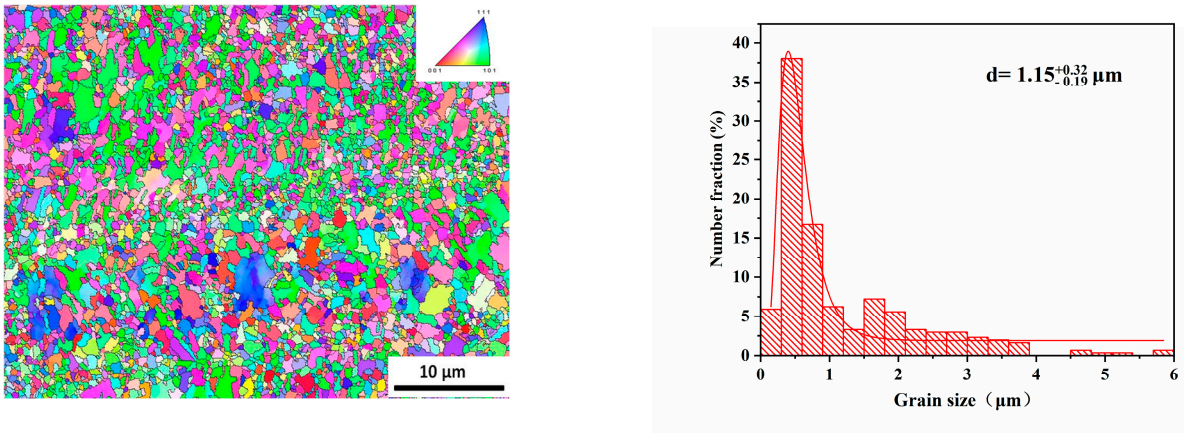


Figure 5. (**a**) EBSD IFP map showing grain morphology and sizes of the matrix, and (**b**) grain size statistical distribution in the CR+AN+AG $CoCrNi_{1.5}Nb_{0.2}$ HEA.

3.2. Mechanical Properties

Figure 6a shows the tensile engineering stress–strain curves of as-CR and CR+AN+AG, together with single-phase coarse-grained $CoCrNi_{1.5}Nb_{0.2}$ HEAs. The YS values of the as-CR, CR+AN+AG, and single-phase coarse-grained $CoCrNi_{1.5}Nb_{0.2}$ HEAs are determined to be 1548, 1409 and 411 MPa, respectively. Figure 6b displays the corresponding tensile true stress (σ)–strain (s) curves, together with the work hardening rate curves (dσ/ds vs. s), where the true strain at dσ/ds = σ corresponds to the UE [56]. The determined UE is marked using circles in Figure 6a, showing a UE of 2.2, 10.1 and 48.8%, and corresponding ultimate tensile strengths (UTS) of 1862, 1611 and 906 MPa, for the as-CR, CR+AN+AG and single-phase coarse-grained $CoCrNi_{1.5}Nb_{0.2}$ HEAs, respectively. The statistical YS, UTS and UE of the as-CR, CR+AN+AG and single-phase coarse-grained $CoCrNi_{1.5}Nb_{0.2}$ HEAs, determined from more than four tensile tests for each of the three alloys, are reported in Table 3. The as-CR, CR+AN+AG and single-phase coarse-grained $CoCrNi_{1.5}Nb_{0.2}$ HEAs exhibit a YS of 1548, 1409 and 411 MPa, a UTS of 1862, 1611 and 906 MPa, and a UE of 2.2, 10.1 and 48.8%, respectively. Compared with the as-CR $CoCrNi_{1.5}Nb_{0.2}$ HEA, on the one hand, the dislocation density significantly decreases and the grain size increases in the CR+AN+AG $CoCrNi_{1.5}Nb_{0.2}$ HEA, reducing the dislocation and GB strengthening; however, on the other hand, precipitation occurs, and two types of precipitates are formed, improving the precipitation's strength. As a result, the strength of the CR+AN+AG $CoCrNi_{1.5}Nb_{0.2}$ HEA slightly decreases relative to that of the as-CR $CoCrNi_{1.5}Nb_{0.2}$ HEA. Compared to the single-phase coarse-grained $CoCrNi_{1.5}Nb_{0.2}$ HEA, precipitation strengthening and significantly enhanced GB strengthening lead to much higher strength in the CR+AN+AG $CoCrNi_{1.5}Nb_{0.2}$ HEA. Figure 6c presents the comparison of the YS and UE of the CR+AN+AG $CoCrNi_{1.5}Nb_{0.2}$ HEA with those of γ'-$L1_2$ and $\gamma''D0_{22}$ coherent precipitate-strengthened HEAs [42,43,57–59], showing a YS of the CR+AN+AG $CoCrNi_{1.5}Nb_{0.2}$ HEA, is superior to those of the γ'-$L1_2$ and γ''-$D0_{22}$ coherent precipitate-strengthened alloys. As shown in Figure 7, the fractography after the tensile tests of the CR+AN+AG $CoCrNi_{1.5}Nb_{0.2}$ HEA is characterized by dimples, suggesting ductile fracture.

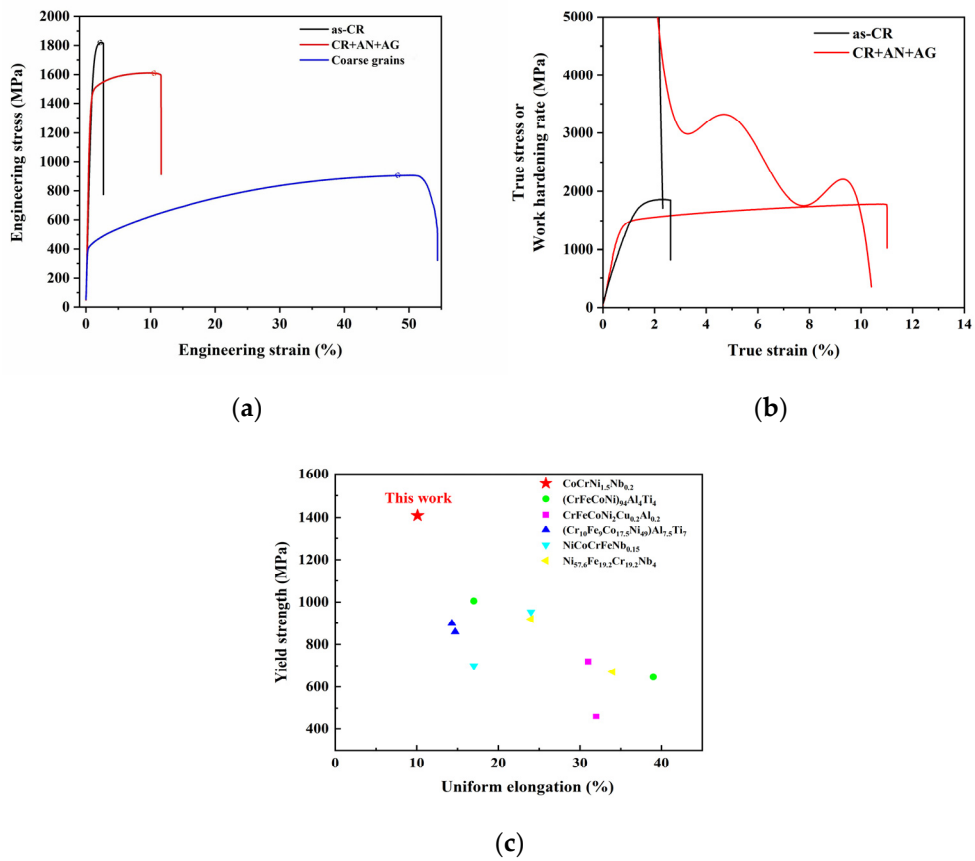


Figure 6. Tensile properties of as-CR and CR+AN+AG, together with single-phase coarse-grained $CoCrNi_{1.5}Nb_{0.2}$ HEAs, coarse grains data from [41]: (**a**) typical engineering stress–strain curves; (**b**) true stress (σ)–strain (s) curves work hardening rate (dσ/ds) curves; (**c**) comparison of YS and UE of CR+AN+AG $CoCrNi_{1.5}Nb_{0.2}$ HEA with those of γ'-$L1_2$ and γ''-$D0_{22}$ coherent precipitate-strengthened HEAs [42,43,57–59].

Table 3. Statistical tensile properties of as-CR and CR+AN+AG $CoCrNi_{1.5}Nb_{0.2}$ HEAs.

Alloys	YS (MPa)	UTS (MPa)	UE (%)	*s* at dσ/d*s* = σ (%)
As-CR	1548 ± 6	1862 ± 7	2.2 ± 0.1	2.2 ± 0.2
CR+AN+AG	1409 ± 11	1611 ± 13	10.1 ± 0.4	9.6 ± 0.2

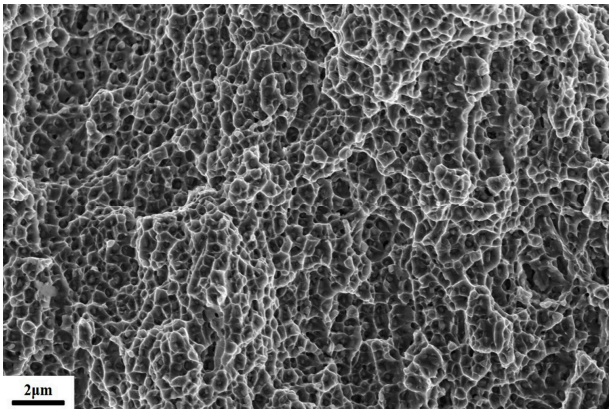


Figure 7. Fractographs of tensile specimens in the CR+AN+AG $CoCrNi_{1.5}Nb_{0.2}$ HEA.

4. Discussion

4.1. Strengthening Mechanisms

For polycrystalline materials, the strengthening mechanism primarily includes solid-solution strengthening (σ_s), dislocation strengthening (σ_d), grain boundary strengthening ($\Delta\sigma_{gb}$) and precipitation strengthening (σ_p). As analyzed in Section 3.1, in CR+AN+AG $CoCrNi_{1.5}Nb_{0.2}$ HEA, the dislocation density is low, and dislocation strengthening can be safely neglected. Therefore, the strengthening mechanisms in CR+AN+AG $CoCrNi_{1.5}Nb_{0.2}$ HEA involve solid-solution strengthening, grain boundary strengthening and precipitation strengthening. Assuming a simple linear superposition of all strengthening mechanisms, the YS (σ_{YS}) of CR+AN+AG $CoCrNi_{1.5}Nb_{0.2}$ HEA can be calculated by the following equation:

$$\Delta\sigma_{YS} = \Delta\sigma_0 + \Delta\sigma_{ss} + \Delta\sigma_{gb} + \Delta\sigma_p \quad (1)$$

where σ_0 is the lattice friction stress (σ_0 = 139 MPa in CoCrNi-based HEAs [41]). $\Delta\sigma_{ss}$, $\Delta\sigma_{gb}$ and $\Delta\sigma_p$ are the contributions of solid-solution, grain boundary and precipitation strengthening, respectively. In a conventional solid solution, solid-solution strengthening is produced by the strain field as a result of a mismatch in atom size between the solvent and solute [60,61]. Nevertheless, in a HEA solid solution, the solvent and solute cannot be distinguished due to equiatomic or near-equiatomic fractions of the constituent elements [62]. To render solid-solution strengthening in HEAs tractable, He et al. [42] proposed that solid-solution strengthening is generated by Nb in an Nb-containing $Ni_2CoCrFeNb_{0.15}$ HEA due to a much larger atomic radius of Nb (1.47 Å [42]) than those of the other four elements (Co 1.25 Å, Cr 1.29 Å, Fe 1.26 Å and Ni 1.25 Å [42]). In the present work, solid-solution strengthening in CR+AN+AG $CoCrNi_{1.5}Nb_{0.2}$ alloys is estimated on the basis of the Nb concentration in the solid-solution matrix. An inspection of the published literature shows that, in the CoCrNi-based HEAs, a dissolution of 1 at% Nb can improve σ_{YS} by 26.1 MPa [41]. Then, $\Delta\sigma_{ss}$ in the CR+AN+AG $CoCrNi_{1.5}Nb_{0.2}$ HEA was calculated based on the Nb concentrations (2.28 at%) in the solid-solution matrix, as reported in Table 2. The contribution of solid-solution strengthening to the YS of CR+AN+AG $CoCrNi_{1.5}Nb_{0.2}$ HEA is estimated as ~60 MPa. The lower contribution of solid-solution strengthening can be attributed to a lower Nb concentration in the solid-solution matrix due to a large amount of Nb precipitating from the matrix to form Nb-rich precipitates. The contribution of GB strengthening can be described by the well-known Hall–Petch equation:

$$\Delta\sigma_{gb} = k\bar{D}^{-1/2} \quad (2)$$

where k is the Hall–Petch slope (k = 840 MPa in CoCrNi-based HEAs) [42] and $\bar{D}$ is the average grain size ($\bar{D}$ = 1.15 μm in CR+AN+AG $CoCrNi_{1.5}Nb_{0.2}$ HEA, as shown in Figure 5b). The contribution of GB strengthening is calculated to be 783 MPa. Then, the contribution of precipitation strengthening is evaluated by: $\Delta\sigma_p = \Delta\sigma_{YS} - \Delta\sigma_0 - \Delta\sigma_{ss} - \Delta\sigma_{gb}$ = 427 MPa. Based on the above calculations, GB strengthening makes a significant contribution to the YS of CR+AN+AG $CoCrNi_{1.5}Nb_{0.2}$ HEA. The high increments caused by GB strengthening can be attributed to fine or ultra-fine grain sizes that result in a high volume of grain boundaries, effectively impeding the dislocation motion. Despite the ultra-fine dimensions of the two precipitates rather than nanoscale sizes, precipitation strengthening still increases the YS significantly, probably due to the high volume fraction of precipitates (total volume fraction of 25%). Additionally, the load-bearing effect of the reinforcement phases, i.e., the two types of precipitates herein, makes an additional contribution to improve the YS [63].

4.2. Ductility

As presented in Table 3, the CR+AN+AG $CoCrNi_{1.5}Nb_{0.2}$ HEA exhibits a high YS (1409 MPa) and UTS (1611 MPa), together with an appreciable UE (10.1%). The follow-

ing factors are likely responsible for good ductility. First, there exists a low density of dislocations in the fine or ultra-fine grains, which facilitates the dislocation motion. Second, despite a relatively high volume fraction (17.4%) of granular (Co, Ni)(Cr, Ni)(Nb, Ni) precipitates, their ultra-fine sizes and granular geometry are beneficial to decrease the stress concentration. Third, despite the length of the lath-shaped ε-(Ni, Co, Cr)$_3$(Nb, Cr) precipitates on the order of micrometers, a semi-coherency between the ε-(Ni, Co, Cr)$_3$(Nb, Cr) precipitates and the matrix reduces the stress concentration.

5. Conclusions

In the present study, the fine or ultra-fine grained $CoCrNi_{1.5}Nb_{0.2}$ HEAs containing a high volume fraction of ultra-fine granular C15 Laves phase (Co, Ni)(Cr, Ni)(Nb, Ni) precipitates and ultra-fine lath-shaped $D0_{19}$-structured ε-(Ni, Co, Cr)$_3$(Nb, Cr) precipitates have been produced by cold rolling plus subsequent annealing at a higher temperature of 900 °C and aging at a lower temperature of 660 °C. The CR+AN+AG $CoCrNi_{1.5}Nb_{0.2}$ HEA exhibits a YS as high as 1409 MPa and a UTS as high as 1611 MPa, accompanied by a UE of 10.1%. The high strength can be primarily attributed to the remarkable grain boundary strengthening of fine or ultra-fine grains and the precipitation strengthening of a high volume fraction of ultra-fine granular (Co, Ni)(Cr, Ni)(Nb, Ni) precipitates and ultra-fine lath-shaped ε-(Ni, Co, Cr)$_3$(Nb, Cr) precipitates, as well as the additional load-bearing effect of the precipitates as reinforcements. The good ductility stems from a low density of dislocations in the fine or ultra-fine grains, ultra-fine sizes, and granular geometry of the (Co, Ni)(Cr, Ni)(Nb, Ni) precipitates, and semi-coherent interfaces between the ε-(Ni, Co, Cr)$_3$(Nb, Cr) precipitates and the matrix.

Supplementary Materials: The following supporting information can be downloaded at: https://www.mdpi.com/article/10.3390/met13050936/s1, Figure S1. Typical engineering stress-strain curves of $CoCrNi_{1.5}Nb_{0.2}$ HEAs cold-rolled + annealed at 800 °C for 1 h, and 1000 °C for 3 min, respectively. Figure S2. Microstructures in the CR+AN+AG $CoCrNi_{1.5}Nb_{0.2}$ HEA: (a) through (c) STEM DF2, DF4 and HAADF micrographs, corresponding to ABF micrograph in Figure 4a.

Author Contributions: Conceptualization, Y.L.; methodology, Y.L. and Z.Y.; software, Z.Y.; validation, Z.Y. and Y.L.; formal analysis, Z.Y.; investigation, Z.Y.; resources, Y.L.; data curation, Z.Y.; writing—original draft preparation, Z.Y.; writing—review and editing, Y.L.; visualization, Y.L.; supervision, Y.L.; project administration, Y.L.; funding acquisition, Y.L. All authors have read and agreed to the published version of the manuscript.

Funding: This research was financially supported by research funding from the Wuhan University of Technology, China, for Newly Recruited Distinguished Professors (grant number: 471-40120281).

Data Availability Statement: The raw and processed data required to reproduce these results are available by contacting the authors.

Conflicts of Interest: The authors declare no conflict of interest.

References

1. Yeh, J.W.; Chen, S.K.; Lin, S.J.; Gan, J.Y.; Chin, T.S.; Shun, T.T.; Tsau, C.H.; Chang, S.Y. Nanostructured high-entropy alloys with multiple principal elements: Novel alloy design concepts and outcomes. *Adv. Eng. Mater.* **2004**, *6*, 299–303. [CrossRef]
2. Rajendrachari, S. An overview of high-entropy alloys prepared by mechanical alloying followed by the characterization of their microstructure and various properties. *Alloys* **2022**, *1*, 116–132. [CrossRef]
3. Pickering, E.J.; Jones, N.G. High-entropy alloys: A critical assessment of their founding principles and future prospects. *Int. Mater. Rev.* **2016**, *61*, 183–202. [CrossRef]
4. Miracle, D.B.; Senkov, O.N. A critical review of high entropy alloys and related concepts. *Acta Mater.* **2017**, *122*, 448–511. [CrossRef]
5. Zhang, J.; Xin, S.; Zhang, Y.; Guo, P.; Sun, H.; Li, T.; Qin, C. Effects of Elements on the Microstructure and Mechanical Properties of AlCoCrFeNiTi High-Entropy Alloys. *Metals* **2023**, *13*, 178. [CrossRef]
6. Rajendrachari, S.; Adimule, V.; Gulen, M.; Khosravi, F.; Somashekharappa, K.K. Synthesis and Characterization of High Entropy Alloy 23Fe-21Cr-18Ni-20Ti-18Mn for Electrochemical Sensor Applications. *Materials* **2022**, *15*, 7591. [CrossRef]

7. Senkov, O.N.; Wilks, G.B.; Scott, J.M.; Miracle, D.B. Mechanical properties of $Nb_{25}Mo_{25}Ta_{25}W_{25}$ and $V_{20}Nb_{20}Mo_{20}Ta_{20}W_{20}$ refractory high entropy alloys. *Intermetallics* **2011**, *19*, 698–706. [CrossRef]
8. Liu, Q.; Liu, X.; Fan, X.; Li, R.; Tong, X.; Yu, P.; Li, G. Designing novel AlCoCrNi eutectic high entropy alloys. *J. Alloys Compd.* **2022**, *904*, 163775. [CrossRef]
9. Yao, H.W.; Qiao, J.W.; Gao, M.C.; Hawk, J.A.; Ma, S.G.; Zhou, H.F.; Zhang, Y. NbTaV-(Ti,W) refractory high-entropy alloys: Experiments and modeling. *Mater. Sci. Eng. A* **2016**, *674*, 203–211. [CrossRef]
10. Lin, Q.; Liu, J.; An, X.; Wang, H.; Zhang, Y.; Liao, X. Cryogenic-deformation-induced phase transformation in an FeCoCrNi high-entropy alloy. *Mater. Res. Lett.* **2018**, *6*, 236–243. [CrossRef]
11. Wu, P.; Gan, K.; Yan, D.; Fu, Z.; Li, Z. A non-equiatomic FeNiCoCr high-entropy alloy with excellent anti-corrosion performance and strength-ductility synergy. *Corros. Sci.* **2021**, *183*, 109341. [CrossRef]
12. Yang, Z.; Yan, D.; Lu, W.; Li, Z. A TWIP-TRIP quinary high-entropy alloy: Tuning phase stability and microstructure for enhanced mechanical properties. *Mater. Sci. Eng. A* **2021**, *801*, 140441. [CrossRef]
13. Tracy, C.L.; Park, S.; Rittman, D.R.; Zinkle, S.G.; Bei, H.; Lang, M.; Ewing, R.C.; Mao, W.L. High pressure synthesis of a hexagonal close-packed phase of the high-entropy alloy CrMnFeCoNi. *Nat. Commun.* **2017**, *8*, 15634. [CrossRef] [PubMed]
14. Hu, G.W.; Zeng, L.C.; Du, H.; Wang, Q.; Fan, Z.T.; Liu, X.W. Combined effects of solute drag and Zener pinning on grain growth of a NiCoCr medium-entropy alloy. *Intermetallics* **2021**, *136*, 107271. [CrossRef]
15. Miao, J.; Guo, T.; Ren, J.; Zhang, A.; Su, B.; Meng, J. Optimization of mechanical and tribological properties of FCC CrCoNi multi-principal element alloy with Mo addition. *Vacuum* **2018**, *149*, 324–330. [CrossRef]
16. Zhao, Y.L.; Yang, T.; Tong, Y.; Wang, J.; Luan, J.H.; Jiao, Z.B.; Chen, D.; Yang, Y.; Hu, A.; Liu, C.T.; et al. Heterogeneous precipitation behavior and stacking-fault-mediated deformation in a CoCrNi-based medium-entropy alloy. *Acta Mater.* **2017**, *138*, 72–82. [CrossRef]
17. Zhang, L.; Du, X.; Zhang, L.; Li, W.; Liang, Y. Achieving ultra-high strength in a precipitation-hardened CoCrNi-based medium-entropy alloy with partially recrystallized microstructure and heterogeneous grains. *Vacuum* **2021**, *188*, 110169. [CrossRef]
18. Liu, X.; Zhang, M.; Ma, Y.; Dong, W.; Li, R.; Lu, Y.; Zhang, Y.; Yu, P.; Gao, Y.; Li, G. Achieving ultrahigh strength in CoCrNi-based medium-entropy alloys with synergistic strengthening effect. *Mater. Sci. Eng. A* **2020**, *776*, 139028. [CrossRef]
19. Li, N.; Gu, J.; Gan, B.; Qiao, Q.; Ni, S.; Song, M. Effects of Mo-doping on the microstructure and mechanical properties of CoCrNi medium entropy alloy. *J. Mater. Res.* **2020**, *35*, 2726–2736. [CrossRef]
20. Murty, B.S.; Yeh, J.W.; Ranganathan, S. *High-Entropy Alloys*; Elsevier: Amsterdam, The Netherlands, 2019.
21. Zhang, Y.; Zuo, T.T.; Tang, Z.; Gao, M.C.; Dahmen, K.A.; Liaw, P.K. Microstructures and properties of high-entropy alloys. *Prog. Mater. Sci.* **2014**, *61*, 1–93. [CrossRef]
22. Chen, J.; Zhou, X.; Wang, W.; Liu, B.; Lv, Y.; Yang, W.; Xu, D.; Liu, Y. A review on fundamental of high entropy alloys with promising high–temperature properties. *J. Alloys Compd.* **2018**, *760*, 15–30. [CrossRef]
23. Li, Z.; Zhao, S.; Ritchie, R.O.; Meyers, M.A. Mechanical properties of high-entropy alloys with emphasis on face-centered cubic alloys. *Prog. Mater. Sci.* **2019**, *102*, 296–345. [CrossRef]
24. Naeem, M.; He, H.; Harjo, S.; Kawasaki, T.; Zhang, F.; Wang, B. Extremely high dislocation density and deformation pathway of CrMnFeCoNi high entropy alloy at ultralow temperature. *Scripta Mater.* **2020**, *188*, 21–25. [CrossRef]
25. Zhao, Y.J.; Qiao, J.W.; Ma, S.G.; Gao, M.C.; Yang, H.J.; Chen, M.W.; Zhang, Y. A hexagonal close-packed high-entropy alloy: The effect of entropy. *Mater. Design.* **2016**, *96*, 10–15. [CrossRef]
26. Hung, P.T.; Kawasaki, M.; Han, J.K.; Lábár, J.L.; Gubicza, J. Thermal stability of a nanocrystalline HfNbTiZr multi-principal element alloy processed by high-pressure torsion. *Mater. Charact.* **2020**, *168*, 110550. [CrossRef]
27. Zhang, T.W.; Ma, S.G.; Zhao, D.; Wu, Y.C.; Zhang, Y.; Wang, Z.H.; Qiao, J.W. Simultaneous enhancement of strength and ductility in a NiCoCrFe high-entropy alloy upon dynamic tension: Micromechanism and constitutive modeling. *Int. J. Plast.* **2020**, *124*, 226–246. [CrossRef]
28. Gludovatz, B.; Hohenwarter, A.; Catoor, D.; Chang, E.H.; George, E.P.; Ritchie, R.O. A fracture-resistant high-entropy alloy for cryogenic applications. *Science* **2014**, *345*, 1153–1158. [CrossRef]
29. Xia, S.Q.; Zhen, W.; Yang, T.F.; Zhang, Y. Irradiation in high entropy alloys. *J. Iron Steel Res. Int.* **2015**, *22*, 879–884. [CrossRef]
30. Lin, Y.S.; Lu, Y.C.; Hsueh, C.H. Strengthening of CoCrNi medium entropy alloy with gadolinium additions. *Vacuum* **2023**, *211*, 111969. [CrossRef]
31. Chang, R.; Fang, W.; Bai, X.; Xia, C.; Zhang, X.; Yu, H.; Liu, B.; Yin, F. Effects of tungsten additions on the microstructure and mechanical properties of CoCrNi medium entropy alloys. *J. Alloys Compd.* **2019**, *790*, 732–743. [CrossRef]
32. Sun, S.J.; Tian, Y.Z.; An, X.H.; Lin, H.R.; Wang, J.W.; Zhang, Z.F. Ultrahigh cryogenic strength and exceptional ductility in ultrafine-grained CoCrFeMnNi high-entropy alloy with fully recrystallized structure. *Mater. Today Nano* **2018**, *4*, 46–53. [CrossRef]
33. Moon, J.; Jang, M.J.; Bae, J.W.; Yim, D.; Park, J.M.; Lee, J.; Kim, H.S. Mechanical behavior and solid solution strengthening model for face-centered cubic single crystalline and polycrystalline high-entropy alloys. *Intermetallics* **2018**, *98*, 89–94. [CrossRef]
34. Agustianingrum, M.P.; Yoshida, S.; Tsuji, N.; Park, N. Effect of aluminum addition on solid solution strengthening in CoCrNi medium-entropy alloy. *J. Alloys Compd.* **2019**, *781*, 866–872. [CrossRef]
35. Wang, Z.; Gao, M.C.; Ma, S.G.; Yang, H.J.; Wang, Z.H.; Ziomek, M.; Qiao, J.W. Effect of cold rolling on the microstructure and mechanical properties of $Al_{0.25}CoCrFe_{1.25}Ni_{1.25}$ high-entropy alloy. *Mater. Sci. Eng. A* **2015**, *645*, 163–169. [CrossRef]

36. Sathiyamoorthi, P.; Basu, J.; Kashyap, S.; Pradeep, K.G.; Kottada, R.S. Thermal stability and grain boundary strengthening in ultrafine-grained CoCrFeNi high entropy alloy composite. *Mater. Des.* **2017**, *134*, 426–433. [CrossRef]
37. Yoshida, S.; Bhattacharjee, T.; Bai, Y.; Tsuji, N. Friction stress and Hall-Petch relationship in CoCrNi equi-atomic medium entropy alloy processed by severe plastic deformation and subsequent annealing. *Scr. Mater.* **2017**, *134*, 33–36. [CrossRef]
38. Yang, M.; Yan, D.; Yuan, F.; Jiang, P.; Ma, E.; Wu, X. Dynamically reinforced heterogeneous grain structure prolongs ductility in a medium-entropy alloy with gigapascal yield strength. *Proc. Natl. Acad. Sci. USA* **2018**, *115*, 7224–7229. [CrossRef]
39. Tong, Y.; Chen, D.; Han, B.; Wang, J.; Feng, R.; Yang, T.; Zhao, C.; Zhao, Y.L.; Guo, W.; Shimizu, Y.; et al. Outstanding tensile properties of a precipitation-strengthened $FeCoNiCrTi_{0.2}$ high-entropy alloy at room and cryogenic temperatures. *Acta Mater.* **2019**, *165*, 228–240. [CrossRef]
40. Pan, Y.; Dong, A.; Zhou, Y.; Du, D.; Wang, D.; Zhu, G.; Sun, B. Enhanced strength-ductility synergy in a novel V-containing γ''-strengthened CoCrNi-based multi-component alloy. *Mater. Sci. Eng. A* **2021**, *816*, 141289. [CrossRef]
41. Zhou, H.; Lin, Y.; Chen, F.; Shen, Q. Effect of Precipitation Behavior on Mechanical Properties of a Nb-Containing CoCrNi-Based High-Entropy Alloy. *Met. Mater. Int.* **2023**, *29*, 674–692. [CrossRef]
42. He, F.; Chen, D.; Han, B.; Wu, Q.; Wang, Z.; Wei, S.; Wei, D.; Wang, J.; Liu, C.T.; Kai, J. Design of $D0_{22}$ superlattice with superior strengthening effect in high entropy alloys. *Acta Mater.* **2019**, *167*, 275–286. [CrossRef]
43. Lu, W.; Luo, X.; Yang, Y.; Le, W.; Huang, B.; Li, P. Co-free non-equilibrium medium-entropy alloy with outstanding tensile properties. *J. Alloys Compd.* **2020**, *833*, 155074. [CrossRef]
44. Xia, G.H.; Ma, Z.L.; Xu, Z.Q.; Wang, M.; Cheng, X.W.; Cai, H.N. Novel high-entropy alloys with high-density ε-$D0_{19}$ and abnormal phase transformation. *Scripta Mater.* **2021**, *199*, 113893. [CrossRef]
45. Hu, G.W.; Zeng, L.C.; Du, H.; Liu, X.W.; Wu, Y.; Gong, P.; Fan, Z.T.; Hu, Q.; George, E.P. Tailoring grain growth and solid solution strengthening of single-phase CrCoNi medium-entropy alloys by solute selection. *J. Mater. Sci. Technol.* **2020**, *54*, 196–205. [CrossRef]
46. Freudenberger, J.; Thiel, F.; Utt, D.; Albe, K.; Kauffmann, A.; Seils, S.; Heilmaier, M. Solid solution strengthening in medium-to high-entropy alloys. *Mater. Sci. Eng. A* **2022**, *861*, 144271. [CrossRef]
47. Liang, Y.J.; Wang, L.; Wen, Y.; Cheng, B.; Wu, Q.; Cao, T.; Xiao, Q.; Xue, Y.; Sha, G.; Wang, Y.; et al. High-content ductile coherent nanoprecipitates achieve ultrastrong high-entropy alloys. *Nat. Commun.* **2018**, *9*, 4063. [CrossRef]
48. Klimova, M.; Shaysultanov, D.; Semenyuk, A.; Zherebtsov, S.; Stepanov, N. Effect of carbon on recrystallised microstructures and properties of CoCrFeMnNi-type high-entropy alloys. *J. Alloys Compd.* **2021**, *851*, 156839. [CrossRef]
49. Semenyuk, A.; Klimova, M.; Shaysultanov, D.; Salishchev, G.; Zherebtsov, S.; Stepanov, N. Effect of nitrogen on microstructure and mechanical properties of the CoCrFeMnNi high-entropy alloy after cold rolling and subsequent annealing. *J. Alloys Compd.* **2021**, *888*, 161452. [CrossRef]
50. Cullity, B.D.; Stock, S.R. *Elements of X-ray Diffraction*, 3rd ed.; Pearson: London, UK, 2001.
51. Gale, W.F.; Totemeier, T.C. *Smithells Metals Reference Book*, 8th ed.; Elsevier: Amsterdam, The Netherlands, 2004.
52. *No.15-0101*; Jonit Committee on Power Diffracction Standards (JCPDS): Swarthmore, PA, USA, 1990.
53. *No.15-0498*; Jonit Committee on Power Diffracction Standards (JCPDS): Swarthmore, PA, USA, 1990.
54. Jiang, H.; Han, K.; Qiao, D.; Lu, Y.; Cao, Z.; Li, T. Effects of Ta addition on the microstructures and mechanical properties of CoCrFeNi high entropy alloy. *Mater. Chem. Phys.* **2018**, *210*, 43–48. [CrossRef]
55. *No.33-0391*; Jonit Committee on Power Diffracction Standards (JCPDS): Swarthmore, PA, USA, 1990.
56. De Hoff, R.T.; Rhines, F.N. *Quantitative Microscopy*; Springer: Berlin/Heidelberg, Germany, 1968.
57. He, J.Y.; Liu, W.H.; Wang, H.; Wu, Y.; Liu, X.; Nieh, T.G.; Lu, Z. Effects of Al addition on structural evolution and tensile properties of the FeCoNiCrMn high-entropy alloy system. *Acta Mater.* **2014**, *62*, 105–113. [CrossRef]
58. Wang, Z.G.; Zhou, W.; Fu, L.; Wang, J.; Luo, R.; Han, X.; Chen, B.; Wang, X.D. Effect of coherent $L1_2$ nanoprecipitates on the tensile behavior of a fcc-based high-entropy alloy. *Mater. Sci. Eng. A* **2017**, *696*, 503–510. [CrossRef]
59. Zhang, L.; Zhou, Y.; Jin, X.; Du, X.; Li, B. Precipitation-hardened high entropy alloys with excellent tensile properties. *Mater. Sci. Eng. A* **2018**, *732*, 186–191. [CrossRef]
60. Courtney, T.H. *Mechanical Behavior of Materials*; Waveland Press: Long Grove, IL, USA, 2005.
61. Argon, A. *Strengthening Mechanisms in Crystal Plasticity*; OUP Oxford: Oxford, UK, 2007.
62. Juan, C.C.; Tseng, K.K.; Hsu, W.L.; Tsai, M.H.; Tsai, C.W.; Lin, C.M.; Chen, S.K.; Lin, S.J.; Yeh, J.W. Solution strengthening of ductile refractory HfMoxNbTaTiZr high-entropy alloys. *Mater. Lett.* **2016**, *175*, 284–287. [CrossRef]
63. Nardone, V.C.; Prewo, K.M. On the strength of discontinuous silicon carbide reinforced aluminum composites. *Scripta Metall.* **1986**, *20*, 43–48. [CrossRef]

Disclaimer/Publisher's Note: The statements, opinions and data contained in all publications are solely those of the individual author(s) and contributor(s) and not of MDPI and/or the editor(s). MDPI and/or the editor(s) disclaim responsibility for any injury to people or property resulting from any ideas, methods, instructions or products referred to in the content.